Prominence detection and chromosphere feature on the prototype RS CVn of active binary systems

Dongtao Cao,[1,2]* Shenghong Gu,[1,2,3]* U. Wolter,[4] M. Mittag,[4] J. H. M. M. Schmitt,[4] Dongyang Gao[5] and Shaoming Hu[5]

[1] *Yunnan Observatories, Chinese Academy of Sciences, Kunming 650216, China*
[2] *Key Laboratory for the Structure and Evolution of Celestial Objects, Chinese Academy of Sciences, Kunming 650216, China*
[3] *School of Astronomy and Space Science, University of Chinese Academy of Sciences, Beijing 101408, China*
[4] *Hamburger Sternwarte, Universität Hamburg, Hamburg D-21029, Germany*
[5] *Shandong Provincial key Laboratory of Optical Astronomy and Solar-Terrestrial Environment, Institute of Space Sciences, Shandong University, Weihai 264209, China*

ABSTRACT

We present a study of high-resolution spectra of RS Canum Venaticorum (RS CVn), a prototype of active binary systems. Our data were obtained from 1998 to 2017 using different telescopes. We analyze the chromospheric activity indicators Ca II IRT, H_α, Na I D_1, D_2 doublet, He I D_3, and H_β using a spectral subtraction technique. The chromospheric emission stems mainly from the K2 IV primary star, while the F5 V secondary star only shows weak emission features in a few of our spectra. We find excess absorption features in the subtracted H_α lines and other activity indicators from spectra taken near primary eclipse, which we ascribe to prominence-like material associated with the primary star. We estimate size limits of these tentative prominences based on the geometry of the binary system, and investigate the physical properties of the strongest prominence. An optical flare, characterized by He I D_3 line emission, together with stronger emission in other activity lines, was detected. The flare energy is roughly comparable to strong flares observed on other RS CVn-type stars. The chromospherically active longitudes of RS CVn most frequently appear near the two quadratures of the system and display changes between observing runs, which indicates an ongoing evolution of its active regions.

Key words: stars: activity – stars: chromospheres – stars: flare – stars: circumstellar matter – stars: binaries: spectroscopic

1 INTRODUCTION

A definition of RS CVn-type binary systems was first performed by Hall (1976) and subsequently refined by Fekel, Moffett, & Henry (1986): a binary system which has at least one cool component showing strong magnetic activity in several forms. This activity manifests itself as strong photometric variability caused by large starspots, chromospheric emission, transition region emission, and coronal radiation. It is commonly accepted that all of these active phenomena arise from a powerful magnetic dynamo generated by the interplay between turbulent motions in the convection zone and the stellar differential rotation. At Yunnan Observatories, we are performing a long-term high-resolution spectroscopic monitoring project that covers several RS CVn-type systems to study their magnetic activity phenomena (e.g. Gu et al. 2002; Cao & Gu 2015; Cao et al. 2019). In the present paper, we focus on the prototype system RS CVn itself.

RS CVn (= HD 114519 = BD+36°2344) is a double-lined, totally eclipsing binary system consisting of a K2 IV primary and a F5 V secondary (Reglero, Gimenez, & Estela 1990; Rodonò, Lanza, & Becciani 2001). The system has a period of about 4.798 days in an almost circular orbit with an inclination of $i = 85°$ (Catalano & Rodonò 1974; Eaton et al. 1993). Table 1 summarizes RS CVn's properties, compiled from Eaton et al. (1993) and Rodonò, Lanza, & Becciani (2001).

RS CVn shows a significant distortion wave in its photometric light curve, caused by starspots on the surface of the K2 IV primary star (e.g. Eaton et al. 1993; Heckert & Ordway 1995; Rodonò, Lanza, & Catalano 1995; Rodonò, Lanza, & Becciani 2001). Based on long-term light curves obtained between 1949 and 1993, Rodonò, Lanza, & Catalano (1995) analyzed its starspot evolution, possible activity cycles and orbital period variations. Rodonò, Lanza, & Becciani (2001) further determined accurate photometric parameters using a long-term sequence of light curves of RS CVn, taking into account the light curve distortions caused by starspots. More recently, using

* E-mail: dtcao@ynao.ac.cn, shenghonggu@ynao.ac.cn

Table 1. RS CVn system parameters.

Parameter	Primary	Secondary
Spectral type	K2 IV	F5 V
$M/M_\odot$	1.44	1.39
$R/R_\odot$	3.85	1.89
Semi-major axis		$16.9R_\odot$
Orbital inclination		$85°$
Orbital period		$4^d.797695$
Mid-primary eclipse $(HJD)^a$		$2, 448, 379.1993$

[a] Primary eclipse is defined as phase zero, where the secondary component is totally eclipsed by the primary one.

Doppler imaging, Xiang et al. (2020) reconstructed the starspot distribution on the primary star and estimated its surface differential rotation based on images derived from two consecutive rotational cycles.

Chromospheric activity of RS CVn has been studied by several authors, e.g. Popper (1988), Reglero, Gimenez, & Estela (1990), Fernández-Figueroa et al. (1986, 1994), and Montes et al. (1996a). RS CVn shows pronounced chromospheric emission in Ca II H & K and other activity lines, the emission features are mainly associated with the K2 IV primary star (Reglero, Gimenez, & Estela 1990; Montes et al. 1996a).

So far, we know only little about the magnetic activity of RS CVn's outer atmosphere, in particular in relation to its chromosphere. Here we present the detection of prominence-like structures on RS CVn and the results of our chromospheric activity study based on the Ca II IRT, H_α, Na I D_1, D_2 doublet, He I D_3, and H_β lines. Our study makes use of a large set of high-resolution spectra obtained during several observing runs between 1998 and 2017. This includes data from a joint observation campaign using telescopes located in China and Mexico in 2017 April, designed to get a dense short-term phase coverage. In Section 2, we provide details of our observations and data reduction. Our analysis of chromospheric activity indicators is described in Section 3. In Section 4, we describe in detail the different activity phenomena of RS CVn during our observations, including prominence-like events, optical flares, and chromospheric activity variations. Finally, we state our conclusions in Section 5.

2 OBSERVATIONS AND DATA REDUCTION

During the runs of Mar. 1998, Feb. 2000, and Feb. 2004, we used the coudé echelle spectrograph (CES, Zhao & Li 2001) mounted on the 2.16-m telescope at the Xinglong station, National Astronomical Observatories, Chinese Academy of Sciences. The spectrograph covered the wavelength range of 5600–9000 Å with an average resolving power of R = $\lambda/\Delta\lambda \simeq 37000$, and the data were recorded on a 1024×1024 pixel CCD. The fiber-fed high-resolution spectrograph HRS was later installed on the 2.16-m telescope, which we used in Jan. 2016 and Nov–Dec. 2017. HRS produces spectra with a resolving power of R $\simeq$ 48000 on a wavelength range of 3900–10000 Å, using a 4096×4096 pixel CCD.

During 2017, Apr 14 to 21, furthermore, we made a joint

Table 2. RS CVn observing log.

Date	HJD (2,450,000+)	Phase	Exp.time (s)
1998 Mar, Xinglong 2.16 m			
1998 Mar 14	0887.3212	0.776	3600
1998 Mar 14	0887.3635	0.785	3600
2000 Feb, Xinglong 2.16 m			
2000 Feb 20	1595.3134	0.346	1800
2000 Feb 20	1595.3352	0.350	1800
2004 Feb, Xinglong 2.16 m			
2004 Feb 03	3039.3954	0.341	3600
2004 Feb 05	3041.2822	0.734	2760
2004 Feb 05	3041.3664	0.752	2400
2004 Feb 07	3043.3250	0.160	3600
2004 Feb 08	3044.3839	0.380	3600
2004 Feb 09	3045.3200	0.576	3600
2016 Jan, Xinglong 2.16 m			
2016 Jan 22	7410.3077	0.385	3600
2016 Jan 23	7411.3284	0.598	3600
2016 Jan 23	7411.3775	0.608	3600
2016 Jan 24	7412.2358	0.787	1800
2016 Jan 24	7412.2889	0.798	1800
2016 Jan 24	7412.3753	0.816	1800
2016 Jan 24	7412.3985	0.821	1800
2016 Jan 25	7413.2727	0.003	1800
2016 Jan 25	7413.3265	0.014	1800
2016 Jan 26	7414.2849	0.214	1800
2016 Jan 26	7414.3373	0.225	1800
2016 Jan 26	7414.3904	0.236	1800
2016 Jan 26	7414.4136	0.241	1800
2016 Jan 28	7416.2773	0.629	1800
2016 Jan 28	7416.3006	0.634	1800
2016 Jan 29	7417.2814	0.838	1800
2016 Jan 29	7417.3048	0.843	1800
2016 Jan 30	7418.3252	0.056	1800
2016 Jan 30	7418.3484	0.061	1800
2016 Jan 30	7418.3718	0.066	1800
2016 Jan 30	7418.3950	0.071	1800
2016 Jan 31	7419.2627	0.251	1800
2016 Jan 31	7419.2859	0.256	1800
2016 Jan 31	7419.3576	0.271	1800
2016 Jan 31	7419.3809	0.276	1800
2017 Apr, Weihai 1 m			
2017 Apr 17	7861.0953	0.344	3600
2017 Apr 18	7862.0654	0.546	3600
2017 Apr 18	7862.1074	0.555	3600
2017 Apr 18	7862.1500	0.564	3600
2017 Apr 18	7862.2457	0.584	3600
2017 Apr 18	7862.2876	0.593	3600
2017 Apr 18	7862.3297	0.601	3600
2017 Apr, TIGRE 1.2 m			
2017 Apr 14	7857.6464	0.625	800
2017 Apr 14	7857.6914	0.635	800
2017 Apr 14	7857.7343	0.644	800
2017 Apr 14	7857.7748	0.652	800
2017 Apr 14	7857.8177	0.661	800
2017 Apr 14	7857.8589	0.670	800
2017 Apr 14	7857.9406	0.687	800
2017 Apr 15	7858.6400	0.832	800
2017 Apr 16	7859.7464	0.063	800
2017 Apr 16	7859.7905	0.072	800

Table 2 – *continued*

Date	HJD (2,450,000+)	Phase	Exp.time (S)
2017 Apr 16	7859.8354	0.081	800
2017 Apr 16	7859.8808	0.091	800
2017 Apr 16	7859.9340	0.102	800
2017 Apr 17	7860.6080	0.243	800
2017 Apr 17	7860.6722	0.256	800
2017 Apr 17	7860.7390	0.270	800
2017 Apr 17	7860.8788	0.299	800
2017 Apr 18	7861.6112	0.452	800
2017 Apr 19	7862.7679	0.693	800
2017 Apr 19	7862.8081	0.701	800
2017 Apr 19	7862.8686	0.714	800
2017 Apr 19	7862.9071	0.722	800
2017 Apr 20	7863.5836	0.863	800
2017 Apr 20	7863.6263	0.872	800
2017 Apr 20	7863.6656	0.880	800
2017 Apr 20	7863.7049	0.888	800
2017 Apr 20	7863.7447	0.896	800
2017 Apr 20	7863.7830	0.904	800
2017 Apr 20	7863.8261	0.913	800
2017 Apr 20	7863.8789	0.924	800
2017 Apr 20	7863.9173	0.932	800
2017 Apr 21	7864.6062	0.076	800
2017 Apr 21	7864.6449	0.084	800
2017 Apr 21	7864.6829	0.092	800
2017 Apr 21	7864.7222	0.100	800
2017 Apr 21	7864.7610	0.108	800
2017 Apr 21	7864.7995	0.116	800
2017 Apr 21	7864.8452	0.126	800
2017 Apr 21	7864.8839	0.134	800
2017 Apr 21	7864.9236	0.142	800
2017 Nov–Dec, Xinglong 2.16 m			
2017 Nov 28	8086.3636	0.298	1800
2017 Nov 28	8086.3868	0.302	1800
2017 Nov 28	8086.4100	0.307	1800
2017 Nov 30	8088.3846	0.719	1800
2017 Nov 30	8088.4078	0.724	1800
2017 Dec 01	8089.3822	0.927	1800
2017 Dec 01	8089.4054	0.932	1800
2017 Dec 07	8095.3590	0.172	1800
2017 Dec 07	8095.3822	0.177	1800
2017 Dec 07	8095.4054	0.182	1800
2017 Dec 08	8096.3461	0.378	1800
2017 Dec 08	8096.3692	0.383	1800
2017 Dec 08	8096.3924	0.388	1800
2017 Dec 08	8096.4156	0.393	1800
2017 Dec 09	8097.3639	0.590	1800
2017 Dec 09	8097.3870	0.595	1800
2017 Dec 09	8097.4104	0.600	1800
2017 Dec 10	8098.3282	0.791	1800
2017 Dec 10	8098.3514	0.796	1800
2017 Dec 10	8098.3746	0.801	1800
2017 Dec 10	8098.3978	0.806	1800
2017 Dec 10	8098.4211	0.811	1800
2017 Dec 11	8099.3624	0.007	1800
2017 Dec 11	8099.3856	0.012	1800
2017 Dec 11	8099.4088	0.017	1800

observation by using the 1-m telescope at the Weihai Observatory of Shandong University, China (Gao et al. 2016) and the TIGRE 1.2-m telescope of Hamburg Observatory, Germany (Schmitt et al. 2014). The Weihai Echelle Spectrograph (WES) is fiber-fed and covers the wavelength range 3800–9000 Å with an average resolving power of R $\simeq$ 50000. TIGRE is a robotic telescope located near Guanajuato in Central Mexico and equipped with the fiber-fed spectrograph HEROS. Its spectra have a resolving power of R $\simeq$ 20000, covering a wavelength range of 3800–5700 Å and 5800–8800 Å in its blue and red arm, respectively.

Table 2 lists our observations of RS CVn, which including the used instrument, the observing date, HJD, orbital phase, and exposure time. The orbital phases were calculated using the ephemerides given in Table 1. Besides our target RS CVn, during each run, we observed a few rapidly rotating early-type stars, used as telluric absorption line templates. Finally, we observed several slowly rotating, inactive stars with the same spectral type and luminosity class as the components of RS CVn. They are required for the spectral subtraction technique described in Section 3.

TIGRE observations are automatically reduced by the TIGRE pipeline (Mittag et al. 2010). We normalized the extracted and wavelength calibrated spectra by using a low-order polynomial fit to the observed continuum with the IRAF[1] package.

All other observations were completely reduced with the IRAF package, following the standard procedures and using Th-Ar spectra of the corresponding nights for wavelength calibration. As a final step, also these spectra were normalized using low-order polynomial fit to the observed continuum.

Some of our observations during Nov–Dec. 2017, obtained at Xinglong, and Apr. 2017 taken by TIGRE, were heavy contaminated by telluric absorption lines in the chromospheric activity regions of interest. We eliminated them using the spectra of two rapidly rotating early-type stars HR 989 (B5 V, $vsini$ = 298 km s^{-1}) and HR 7894 (B5 IV, $vsini$ = 330 km s^{-1}), respectively, with an interactive procedure in the IRAF package.

Examples of the Ca II IRT, H$_\alpha$, Na I D$_1$, D$_2$ doublet, He I D$_3$, and H$_\beta$ line profiles of RS CVn are displayed in Figure 1.

3 ANALYSIS OF CHROMOSPHERIC ACTIVITY INDICATORS

We simultaneously analyze different chromospheric activity indicators, namely Ca II IRT, H$_\alpha$, Na I D$_1$, D$_2$ doublet, He I D$_3$, and H$_\beta$ lines, formed in a wide range of atmospheric heights. To separate the contribution from the photosphere absorption profile in these lines, we apply a spectral subtraction technique, making use of the STARMOD program (Barden 1985; Montes et al. 1997, 2000). STARMOD synthesizes a spectrum, later subtracted, by rotationally broadening, RV-shifting, and adaptively weighting spectra of two suitable template stars. These template stars are chosen as

---

[1] IRAF is distributed by the National Optical Astronomy Observatories, which is operated by the Association of Universities for Research in Astronomy (AURA), Inc., under cooperative agreement with the National Science Foundation.
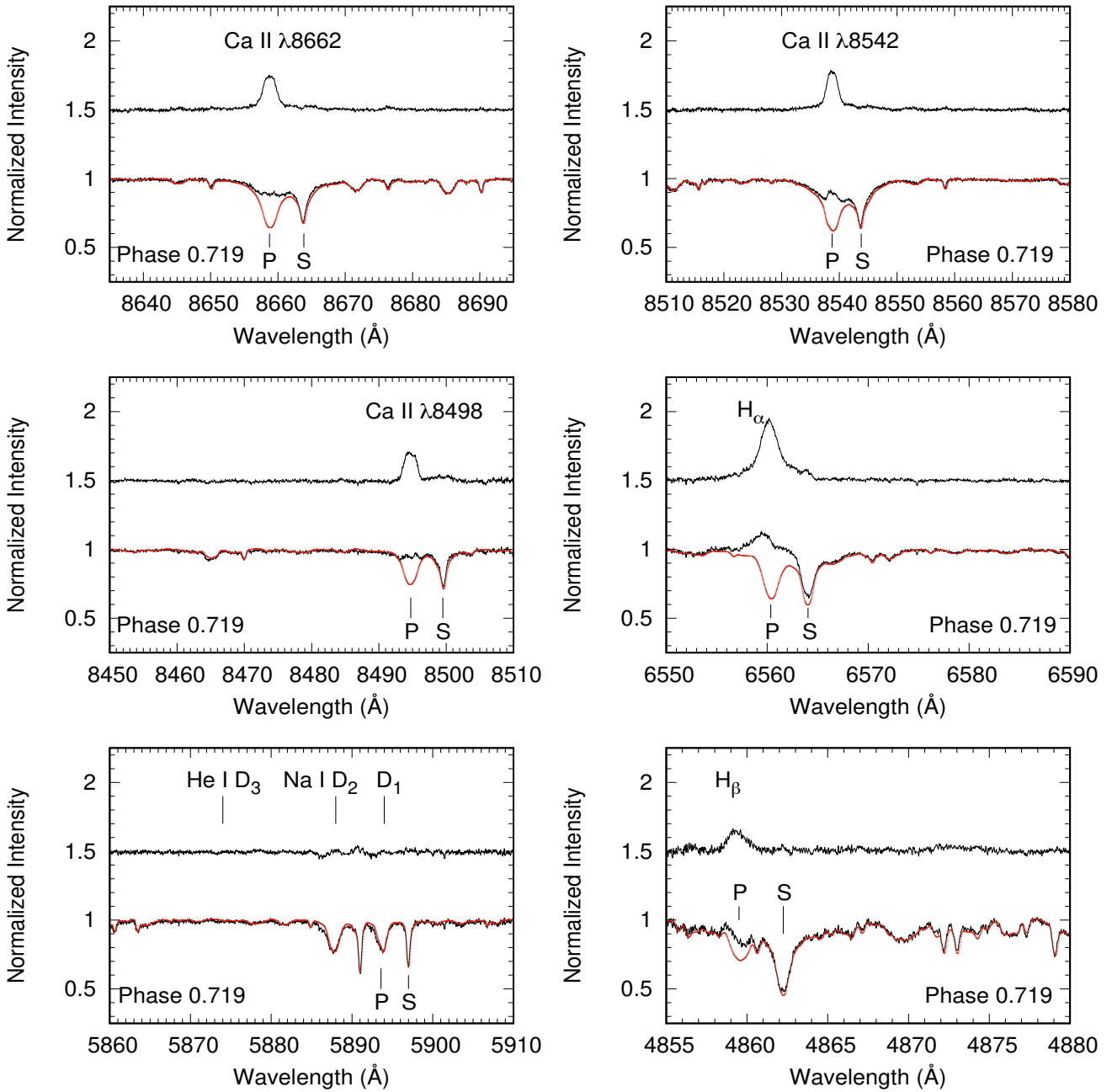
Figure 1. Example of the observed, synthesized, and subtracted spectra for the annotated spectral line regions, shown for one spectrum obtained at at Xinglong (2017 Nov 30). In each panel, the lower solid-line indicates the observed spectrum, the dotted red line represents the synthesized spectrum constructed from spectra of two template stars, and the upper graph shows the resulting subtraction spectrum, shifted for better visibility. "P" and "S" mark the positions of the chromospheric activity lines for the primary and secondary components of RS CVn, respectively.

inactive, but having the same spectral-type and luminosity class as the components of the system. Thus, the synthesized spectrum approximates the non-active state of the binary, and the subtraction between the observed and synthesized spectra produces the activity contribution as excess emission and/or absorption, relative to the presumed inactive state.

For the observations of Jan. 2016 and Nov–Dec. 2017, taken at Xinglong, we use spectra of HR 8088 (K2 IV) and HR 3262 (F6 V) as templates for the primary and secondary star, respectively. The $vsini$ of each binary component is determined by STARMOD using these template spectra, resulting in an average $vsini$ of $45\,\mathrm{km\,s^{-1}}$ for the primary star and $14\,\mathrm{km\,s^{-1}}$ for the secondary one, based on a high signal-to-noise ratio (SNR) spectral window spanning many photospheric absorption lines, observed at phases where the two components of the system are well separated. The obtained $vsini$ values are in good agreement with the results of $42 \pm 3\,\mathrm{km\,s^{-1}}$ & $11 \pm 2\,\mathrm{km\,s^{-1}}$ estimated by Strassmeier & Fekel (1990), and $44.9 \pm 1\,\mathrm{km\,s^{-1}}$ & $12.4 \pm 0.5\,\mathrm{km\,s^{-1}}$ by Xiang et al. (2020). The adopted intensity ratios (primary/secondary) used by

STARMOD are 0.57/0.43 for the Ca II λ8662 spectral region, 0.56/0.44 for the Ca II λ8542 spectral region, 0.55/0.45 for the Ca II λ8498 spectral region, 0.5/0.5 for the H$_\alpha$ spectral region, 0.47/0.53 for the Na I D$_1$ and D$_2$ doublet, He I D$_3$ spectral region, finally 0.43/0.57 for the H$_\beta$ spectral region.

The same template stars, HR 8088 and HR 3262, are also used for the observations of Apr. 2017, obtained at Weihai, as well as the observations of Mar. 1998, Feb. 2000, and Feb. 2004 obtained at Xinglong. We use the same *vsini* values and intensity weight ratios as given above, with the exception of the H$_\beta$ line region for the Weihai observations, because of very low SNR, and the Xinglong observations, where the line is not covered. Also, during the 1998 observing run, the Ca II λ8498 line was not covered by the spectra due to an echelle setup change.

Because the template stars used above were not observed by the TIGRE telescope, we use spectra of two other inactive stars HR 5227 (K2 IV) and HR 8697 (F6 V) as templates instead. The *vsini* values of 45 & 14 km s^{-1} are used, and the resulting and adopted intensity weight ratios are 0.59/0.41 for the Ca II IRT spectral region, 0.51/0.49 for the H$_\alpha$ spectral region, and 0.44/0.56 for the H$_\beta$ spectral region. Also for some of the TIGRE observations, H$_\beta$ could not be analyzed because of too low SNRs.

During eclipses of RS CVn's components, the intensity weights of the two components change with orbital phase, and the line profiles are distorted – a situation that STARMOD can not model. Since some of our observations were obtained during eclipse, the resulting spectra have been excluded from our analysis, they are not listed in Table 1. This applies with the exception of spectra observed during total primary eclipse, i.e. when the secondary is completely occulted by the primary, such as observations on 2017 Dec 11. In these cases, we do use the template spectrum of the K2 IV alone to perform our analysis.

As a typical example, we show the chromospherically sensitive lines of one spectrum and illustrate the above described processing in Fig. 1. As expected, RS CVn shows pronounced chromospheric emission in all analyzed lines, mainly associated with the primary star. Moreover, for several observations of 2017 November–December and some observations of other observing runs, there are obvious excess emission features associated with the secondary star of RS CVn in the subtracted spectra (especially in the H$_\alpha$ line), which indicates that the secondary star is also active in the system, although much weaker.

The equivalent widths (EWs) of the subtracted Ca II IRT, H$_\alpha$, and H$_\beta$ line profiles are measured with the SPLOT task in the IRAF package, as described in our previous papers (Cao & Gu 2015, 2017), they are summarized in Table A together with their estimated uncertainties, where we also provide the ratios of the EW(λ8542)/EW(λ8498) and the E$_{H\alpha}$/E$_{H\beta}$ for some of our observations. The E$_{H\alpha}$/E$_{H\beta}$ ratios are calculated from the EW(H$_\alpha$)/EW(H$_\beta$) values with the correction:

$$\frac{E_{H\alpha}}{E_{H\beta}} = \frac{EW(H_\alpha)}{EW(H_\beta)} * 0.2444 * 2.512^{(B-R)} \tag{1}$$

given by Hall & Ramsey (1992), which takes into account the absolute flux density in H$_\alpha$ and H$_\beta$ lines, and the color index; we use $B - R = 0.81$ for the calculation here.

The EW$_{8542}$/EW$_{8498}$ ratios thus obtained lie in the range of 1.0–2.5, consistent with the ratios found in solar plages (∼1.5–3; Chester 1991) as well as several other chromospherically activity stars (e.g. Montes et al. 2000; Gu et al. 2002; Cao & Gu 2015; Cao et al. 2020), thereby suggesting that the Ca II IRT line emission arises predominantly from plage-like regions.

4 RESULTS AND DISCUSSION

4.1 Prominence-like absorption features

4.1.1 Excess absorption features

At phases near primary eclipse, some of our RS CVn spectra show excess absorption features, visible in the STARMOD-subtracted spectral profiles, most strongly in the Balmer lines.

As shown in Fig. 2, for the observations on 2017 December 01 at phases 0.927 and 0.932, shortly before the primary star began to eclipse the secondary one, an excess absorption feature appeared in the red wing of the subtracted H$_\alpha$ and H$_\beta$ line profiles. Simultaneously, an absorption feature appeared in the He I D$_3$ line region, in both the observed and subtracted spectra. We had previously observed similar absorption features in the same lines of the RS CVn-type star SZ Psc (Cao et al. 2019, 2020).

From Fig. 3, moreover, it can be seen that there were excess absorption features presented in the blue wing of the subtracted H$_\alpha$ line profile at several phases on 2017 April 16, and again on 2017 April 21. These absorption features again occurred at orbital phases just after primary eclipse, when the projected separation between two components gradually becomes larger, repeating after one orbital cycle. In the subtracted spectra, furthermore, we note that the intensity of excess absorption gradually decayed until the features disappeared (indicated by the arrows in Fig. 3). Different from what we found on 2017 December 01, however, there were no significant excess absorption features in the blue wings of H$_\beta$ line, probably because of much lower SNRs.

We attribute these excess absorption features to prominence-like material associated with the primary star, thereby absorbing radiation from the secondary star near the primary eclipse. This occurs during these phases because the materials lie near the secondary star in velocity space, which, in turn, is located behind the primary star along the line of our sight. Stellar prominences have been detected as transient absorption features passing through the rotationally broadened H$_\alpha$ line profiles on a number of rapidly rotating single stars such as AB Dor (Collier Cameron & Robinson 1989), Speedy Mic (Jeffries 1993; Dunstone et al. 2006a; Wolter et al. 2008), HK Aqr (Byrne, Eibe, & Rolleston 1996), RE 1816+514 (Eibe 1998), PZ Tel (Barnes et al. 2000), and RX J1508.6–4423 (Donati et al. 2000). Transient absorption features are thought to originate from cool clouds of mostly neutral material, magnetically supported above the stellar photosphere and forced to corotate with the star in a manner reminiscent of solar prominences, which then scatter the underlying chromospheric emission out of the line of sight as they transit the stellar disk (Collier Cameron & Robinson 1989).
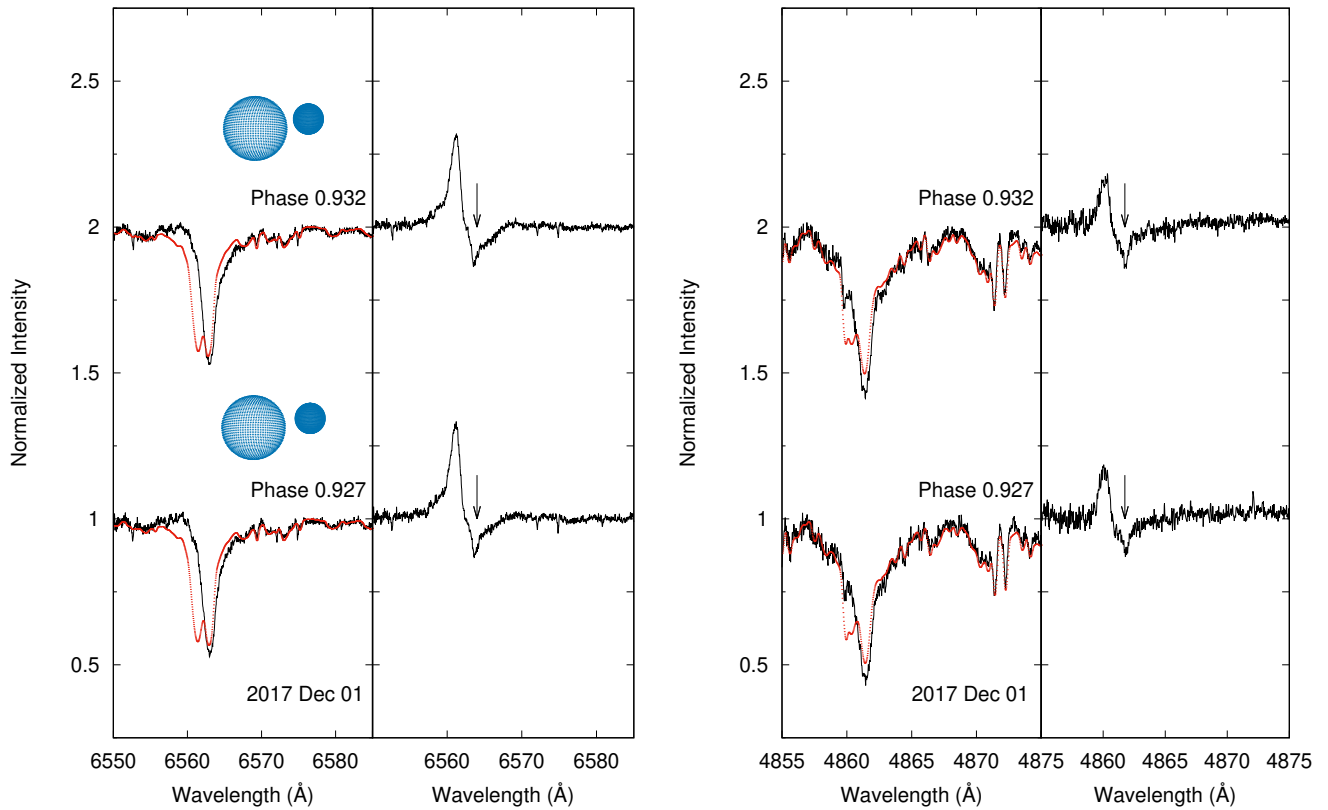
Figure 2. Excess absorption features in H$_\alpha$ (left panel) and H$_\beta$ (right panel), observed at phases 0.927 and 0.932 on 2017 December 1. The left side of each panel shows the observed (solid) and synthesized (dotted) spectra, while the right side contains the subtracted spectra. The geometry of the system at each phase is also shown. Arrows indicate excess absorption features in the subtracted spectra.

Actually, Balmer excess absorptions, interpreted in terms of prominence-like features, have even been detected in several RS CVn-type stars, mainly double-lined eclipsing binary systems (Hall et al. 1990; Hall & Ramsey 1992; Frasca et al. 2000; Cao et al. 2019, 2020). Furthermore, we detected such features several times in the RS CVn-type binary star SZ Psc (Cao et al. 2019, 2020), including cases apparently caused by flare-related prominence activation and post-flare loops (Cao et al. 2019).

The $E_{H\alpha}/E_{H\beta}$ values have repeatedly been used as diagnostics for discriminating between prominence-like and plage-like structures. Huenemoerder & Ramsey (1987) found that low ratios in RS CVn-type stars are caused by plage-like regions, while prominence-like structures have high values. Buzasi (1989) also developed a NLTE radiative transfer model and concluded that the low ratios ($\sim$ 1–2) could be achieved both in plages and prominences viewed against the disk, but high values ($\sim$ 3–15) could only be achieved in prominence-like structures viewed off the stellar limb. For RS CVn, the ratios we have obtained are in the range of 1–3 for most of our observations (see Table A), which suggests that there are plage-like regions in the chromosphere, in agreement with the results of the EW$_{8542}$/EW$_{8498}$. There are much higher $E_{H\alpha}/E_{H\beta}$ values for the observations at phase 0.927 and 0.932 during 2017 Nov–Dec, which exhibit excess absorption features in the subtractions, this should be because of prominence-like structure.

On the other hand, for the excess absorptions present in

the subtracted H$_\alpha$ lines near primary eclipse in 2017 April, the $E_{H\alpha}/E_{H\beta}$ ratios are not high. Furthermore, the excess H$_\alpha$ absorptions are not strong here and no obvious excess absorptions appear in H$_\beta$, though potentially hidden by low SNRs. This implies that the prominence activity was much weaker during those observations.

4.1.2 Prominence heights

Since the geometry of RS CVn is well established, we can try to infer approximate limits on the physical extent of prominences, using the parameters listed in Table 1. For the excess absorption features observed on 2017 April 16 and 21, both of them appeared and disappeared around a similar phase (see Fig. 3). Large stellar prominences may have lifetimes spanning several stellar rotations (Donati et al. 1999), therefore, both can be expected to be caused by the same prominence. At phase 0.102 on 2017 April 16, the projected separation between the limbs of the two stellar components is about 4.32 $R_\odot$, which suggests that the prominence extends at least up to this value from the surface of the primary star. Furthermore, the separation between the limbs of the two components is about 0.74 $R_\odot$ at phase 0.063, and therefore the separation between the leading limb of the primary star and the far limb of the secondary star is 0.74 $R_\odot$ + 2 * R_{sec} = 4.52 $R_\odot$, which can also be regarded as the upper limit on the prominence's height from the sur-
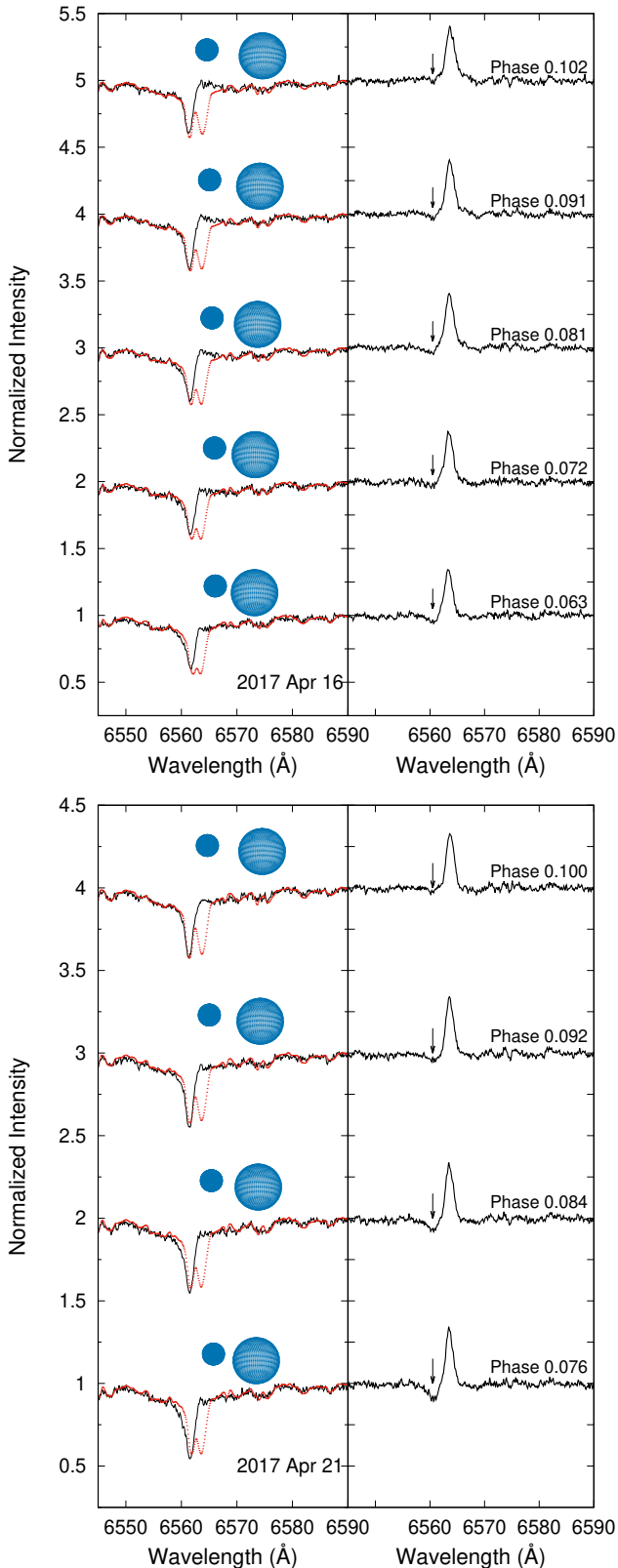
Figure 3. Same as Fig. 2, for excess absorption features in the H_α line profiles observed on 2017 April 16 (top) and 21 (bottom).

face of the primary, which would still allow it to be projected on the stellar disk of the secondary. Hence, we conclude that this prominence probably extends from the surface of the primary star in the range between 4.32 $R_\odot$ ($\simeq 1.12\ R_{pri}$) and 4.52 $R_\odot$ ($\simeq 1.17\ R_{pri}$).

Following the same line of reasoning, for the excess absorption detected on 2017 December 1, the separation between the limbs of the two system components at phase 0.927 is about 1.74 $R_\odot$ in the plane of the sky, which again means that the prominence extends at least up to this height above the surface of the primary. At phase 0.932, the separation between the limbs of the two components is about 1.28 $R_\odot$ and the separation between the leading limb of the primary and the far limb of the secondary is 1.28 $R_\odot + 2 * R_{sec} = 5.06\ R_\odot$. To summarize, this prominence structure probably extends from the surface of the primary star somewhere between 1.74 $R_\odot$ ($\simeq 0.45\ R_{pri}$) and 5.06 $R_\odot$ ($\simeq 1.31\ R_{pri}$).

In single stars, stellar prominences reach heights of several stellar radii, they usually lie near or beyond the corotation radius. For example, the distances of many prominences from the stellar rotation axis are mainly between 3 and 5 stellar radii for the star AB Dor with the corotation radius at 2.7 stellar radii (Collier Cameron & Robinson 1989). For the primary star of RS CVn, however, its Keplerian corotation radius ($R_k = \sqrt[3]{GM/\Omega^2}$) is calculated to be about 3.3 R_{pri} (2.3 R_{pri} from the surface). Therefore, according to our estimate, prominence-like structures of RS CVn appear to be formed within the corotation radius of the primary star, indicating a different behavior, compared to stellar prominences in single stars.

4.1.3 Prominence column density and mass

The prominence detected on 2017 December 01 can be seen both in the H_α and H_β lines, it is much stronger than its 2017 April counterpart. Here we characterize the physical properties of this stronger prominence.

Assuming a prominence temperature of roughly 10,000 K, hence a thermal Doppler velocity of hydrogen of 12.0 km/s, furthermore assuming a random turbulent velocity of about 5 km/s, Dunstone et al. (2006b) used the curve of growth method to obtain the column densities of H_α in the n = 2 level and of singly ionized Ca II atoms in the ground state. They then used the hydrogen-to-calcium ratio in solar prominences to obtain the column density of hydrogen atoms in the ground state. In this way they derived column densities of prominences on Speedy Mic in the n = 2 level of hydrogen with a mean value of $logN_2 = 18.61 \pm 0.05$ m^{-2} and in the ground state with a mean value of $logN_1 = 23.38 \pm 0.11$ m^{-2}.

Since no Ca II H&K measurements available, we adopt a different strategy, following Leitzinger et al. (2016). These authors used the determined ratio of EW(H_β)/EW(H_α) (~ 0.37) in prominence absorptions to estimate the logarithmic hydrogen column density for the state N_2 from the curve of growth given in Dunstone et al. (2006b) and tentatively applied the N_1-to-N_2 ratio of Speedy Mic to their target to derive the column density of hydrogen atoms in the ground state. They derived $logN_2$ and $logN_1$ values of about 18.0 m^{-2} and 23.7 m^{-2} on the fast rotating dMe star HK Aqr, respectively.
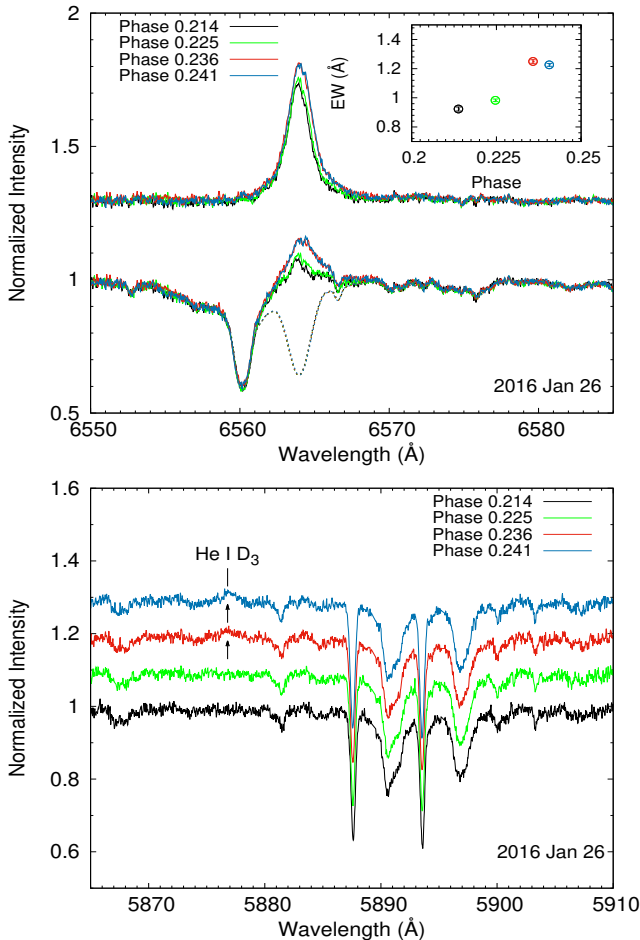
Figure 4. H_α (top) and He I D_3 (bottom) line profiles at the annotated phases, observed on 2016 January 26. In the top panel the subtracted spectra are shifted for better visibility. Corresponding EW variations of the subtracted H_α profiles are shown in the inset. In the bottom panel, the observed He I D_3 line profiles are arranged and shifted in order of increasing phase. Arrows indicate notable He I D_3 line emission features.

To measure EWs of prominence absorptions in our H_α and H_β profiles, we fit the subtracted spectra with multi-Gaussian profiles and then identify the Gaussian absorption component as the prominence and the Gaussian emission component as the chromospheric activity. In this way we obtained a ratio EW(H_β)/EW(H_α) of about 0.33 and derive a $logN_2$ of about 17.6 m^{-2} from the curve of growth of Dunstone et al. (2006b). We then derived a $logN_1$ of about 22.4 m^{-2} through adopting the N_1 to N_2 ratio of Speedy Mic. These values are slightly smaller than those found by Dunstone et al. (2006b) and Leitzinger et al. (2016) for their target stars.

Now, having obtained the column density in the ground state of hydrogen, we can calculate the mass of prominence by using $M = m_H N_1 A$, where m_H is the mass of a hydrogen atom and A is the projected area of the prominence. Again, we follow the method in Dunstone et al. (2006b) and Leitzinger et al. (2016) to estimate the projected prominence area. If the prominence is optically thick, when transiting the center of the stellar disk, the flux fraction of the prominence absorption can be used to calculate the fraction of the star

obscured by the prominence (see the equation (3) given in Leitzinger et al. 2016). For our situation, by comparing the EW(H_β)/EW(H_α) ratio to the theoretical curve of growth of Dunstone et al. (2006b), it can be seen that the ratio is close to the saturated part of the theoretical curve and therefore the assumption of the optically thick case seems justified. Different from Speed Mic and HK Aqr, RS CVn is a binary and therefore the visible background area is the sum of two components of the system. We have calculated a mass of 2.7×10^{15} kg for hydrogen of this prominence, which is slightly larger than the values of prominences in single active stars, which are in the range of $2-6 \times 10^{14}$ kg for AB Dor (Collier Cameron et al. 1990), $0.5-2.3 \times 10^{14}$ kg for Speedy Mic (Dunstone et al. 2006b), and 5.7×10^{13} kg for HK Aqr (Leitzinger et al. 2016). Our result may be reasonable, because close binary stars are usually more active than single stars and the stronger prominence absorption found in RS CVn implies prominence material with more mass.

4.2 Flare event

Similar to the solar case, stellar flares are powerful and explosive phenomena in the outer atmosphere, commonly believed to be caused by the energy released in magnetic reconnections (Schrijver & Zwaan 2000). Flares can be observed across the entire electromagnetic spectrum from shorter X-ray to longer radio wavelengths. Due to its very high excitation potential, the He I D_3 line is an important indicator to trace flare activity in solar and stellar chromospheres. He I D_3 shows obvious emission features above the continuum level during an optical flare, as widely observed on the Sun (Zirin 1988) and in several RS CVn-type stars like II Peg (Huenemoerder & Ramsey 1987; Montes et al. 1997; Berdyugina, Ilyin, & Tuominen 1999; Frasca et al. 2008), V711 Tau (García-Alvarez et al. 2003; Cao & Gu 2015), UX Ari (Montes et al. 1996b; Gu et al. 2002; Cao & Gu 2017), DM UMa (Zhang et al. 2016) and SZ Psc (Cao et al. 2019, 2020).

Some consecutive H_α and He I D_3 line profiles observed on 2016 January 26 are shown in Fig. 4. It can be seen that the H_α line profile shows a significant increase by a factor of about 1.3 from phase 0.225 to 0.236, and simultaneously the He I D_3 line changes to emission during this phase interval. Simultaneously, other chromospheric lines also show a strengthened emission. Taking into consideration these combined facts, a flare event was detected during this night.

According to the measured EWs of the excess H_α emission, the observation at phase 0.236 may well correspond to the flare maximum (as also seen in Fig. 4). We compute the stellar continuum flux F_{H_α} (in erg cm^{-2} s^{-1} Å^{-1}) near H_α as a function of the color index $B - V$ (~ 0.621 for RS CVn; Messina 2008) based on the empirical relationship

$$\log F_{H_\alpha} = [7.538 - 1.081(B - V)] \pm 0.33$$
$$0.0 \leq B - V \leq 1.4 \quad (2)$$

of Hall (1996), and then convert the EW into an absolute surface flux F_S (in erg cm^{-2} s^{-1}). Therefore, the flare emits 1.66×10^{31} erg s^{-1} at flare maximum in H_α, which is derived by converting the absolute surface flux into luminosity. During above calculation, we have corrected the EW to

the total continuum before conversion to absolute flux at the stellar surface, and we assume that the flare occurred on the primary, since the intensity enhancement was associated with this star (see Fig. 4). The energy released in the H_α line is of similar order of magnitude as strong flares on other highly active RS CVn-type stars, such as V711 Tau (Cao & Gu 2015), UX Ari (Montes et al. 1996b; Gu et al. 2002; Cao & Gu 2017), HK Lac (Catalano & Frasca 1994), and SZ Psc (Cao et al. 2019, 2020).

We note that, as visible in Fig. 4, during the increasing phase of the flare, the excess H_α emission profile shows a red asymmetry, i.e. the increase on the red side of the profile is stronger than on the blue, most pronounced from phase 0.225 to 0.236. This feature had also been observed during flares in the active stars PW And (López-santiago et al. 2003) and LQ Hya (Montes et al. 1999). To our knowledge, the red asymmetry is frequently seen in chromospheric activity lines during solar flares, and usually believed to result from chromospheric downward condensations (Canfield et al. 1990).

4.3 EW variations and active longitudes

The observing runs of Jan. 2016 at Xinglong, Apr. 2017 by the TIGRE and Weihai telescopes, as well as Nov–Dec. 2017 again at Xinglong had a denser orbital phase coverage than our earlier observations. We group those observations together to analyze a possible rotational modulation of activity, and therefore jointly analyze the EWs of H_α, H_β, and Ca II IRT line subtractions as a function of orbital phase.

As shown in Fig. 5, the EW variations of the different chromospheric activity indicators are closely correlated. In 2016 January, the most striking feature is the pronounced enhancement in chromospheric emission around the first quadrature of the system, because there is a strong optical flare as discussed in Section 4.2, which possibly indicates that an active longitude exists here. For the 2017 April observing run, there are two active longitudes appearing near the two quadratures of the system where the first active longitude is stronger than the second one. For the 2017 November–December observations, the overall feature of the chromospheric variation is flat during the first half of the orbital phase, but a relatively strong active longitude appears near the second quadrature.

Therefore, the chromospherically active longitudes of RS CVn most frequently appear near the two quadratures of the system and show changes between observing runs. Similar findings were also made in other chromospheric activity stars (e.g. Zhang & Gu 2008; Cao et al. 2020). Based on the same datasets, moreover, Xiang et al. (2020) reconstructed surface spot maps of the primary star using Doppler imaging. The surface maps of 2016 January and 2017 April show that there are strong spot groups around phase 0.25, which are spatially associated with the chromospheric activity longitudes identified here.

5 SUMMARY AND CONCLUSIONS

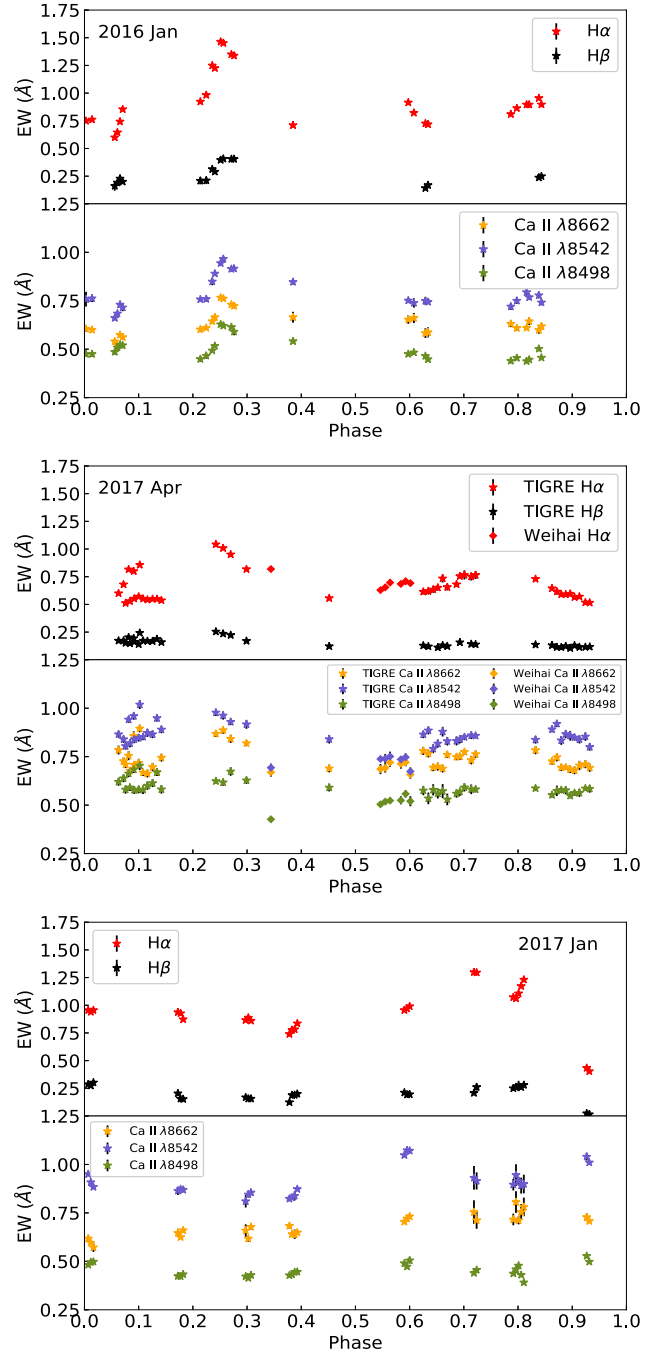Based on the above analysis, our main results are:

Figure 5. EWs of the subtracted Ca II IRT, H_α, and H_β line profiles versus orbital phase, the corresponding observing runs are marked in each panel.

(i) RS CVn shows excess emission features in the Ca II IRT, H_α, and H_β lines, and the chromospheric emission stems mainly from the K2 IV primary of the system, which agrees to previous results reported by other authors. In addition, the F5 V secdonary shows weak chromospheric emission in some of our observations, implying an active, albeit much less active, chromosphere on this star, too.

(ii) There are some unusual excess absorption features in the subtracted spectra taken near primary eclipse, which appear to be caused by two prominences located on the primary

star. These tentative prominences absorb radiation from the secondary star at phases near primary eclipse. We have investigated the physical properties of the prominence structure based on the absorption features and the geometry of RS CVn. Two prominences are estimated to have heights of 1.12 R_{pri} – 1.17 R_{pri} and 0.45 R_{pri} – 1.31 R_{pri} above the surface of the primary star, respectively. Moreover, we characterize the stronger to get a mass of 2.7 $\times$ 10^{15} kg for hydrogen.

(iii) An optical flare was detected on 2016 January 26, most strongly indicated by the He I D_3 line emission feature. The energy released in the H_α line during flare maximum, 1.66×10^{31} erg s^{-1}, has a similar order of magnitude as strong flares of other very active RS CVn-type stars.

(iv) RS CVn shows rotational modulation of chromospheric activity, which means the presence of the chromospheric activity longitudes over the surface of the primary star. The active longitudes most frequently appear around the two quadratures of the binary system.

DATA AVAILABILITY

The data underlying this article are available from the authors upon request.

REFERENCES

Barden S. C., 1985, ApJ, 295, 162
Barnes J. R., Collier Cameron A., James D. J., Donati J.-F., 2000, MNRAS, 314, 162
Berdyugina S. V., Ilyin I., Tuominen I., 1999, A&A, 349, 863
Buzasi D. L., 1989, PhD thesis, Pennsylvania State Univ.
Byrne P. B., Eibe M. T., Rolleston W. R. J., 1996, A&A, 311, 651
Canfield R. C., Kiplinger A. L., Penn M. J., Wülser J.-P., 1990, ApJ, 363, 318
Catalano S., Frasca A., 1994, A&A, 287, 575
Catalano S., Rodonò M., 1974, PASP, 86, 390

Cao D. T., Gu S. H., 2015, MNRAS, 449, 1380
Cao D. T., Gu S. H., 2017, RAA, 17, 055
Cao D. T. et al., 2019, MNRAS, 482, 988
Cao D. T. et al., 2020, AJ, 159, 292
Chester M. M., 1991, PhD thesis, Pennsylvania State Univ
Collier Cameron A., Robinson R. D., 1989, MNRAS, 236, 57
Collier Cameron A. et al., 1990, MNRAS, 247, 415
Donati J.-F. Collier Cameron A., Hussain G. A., Semel M., 1999, MNRAS, 302, 437
Donati J.-F. et al., 2000, MNRAS, 316, 699
Dunstone N. J., Barnes J. R., Collier Cameron A., Jardine M., 2006a, MNRAS, 365, 530
Dunstone N. J., Collier Cameron A., Barnes J. R., Jardine M., 2006b, MNRAS, 373, 1308
Eaton J. A., Henry G. W., Bell C., Okorogu A., 1993, AJ, 106, 1181
Eibe M. T., 1998, A&A, 337, 757
Fekel F. C., Moffett T. J., Henry G. W., 1986, ApJS, 60, 551
Fernández-Figueroa M. J., Montes D., de Castro E., Cornide M., 1994, ApJS, 90, 433F
Fernández-Figueroa M. J. et al., 1986, A&A, 169,219
Frasca A., Marino G., Catalano S., Marilli E., 2000, A&A, 358, 1007
Frasca A., Biazzo K., Taş G., Evren S., Lanzafame A. C., 2008, A&A, 479, 557
Gao D.-Y. et al., 2016, PASP, 128, 125002
García-Alvarez, D. et al., 2003, A&A, 397, 285
Gu S.-H., Tan H.-S., Shan H.-G., Zhang F.-H., 2002, A&A, 388, 889
Hall D. S., 1976, in Fitch W. S., ed, Multiple Periodic Variable Stars, IAU Coll. 29. Reidel: Dordrecht, p. 287
Hall J. C., 1996, PASP, 108, 313
Hall J. C., Ramsey L. W., 1992, AJ, 104, 142
Hall, J. C., Huenemoerder D. P., Ramsey, L. W., Buzasi D. L., 1990, ApJ, 358, 610
Heckert P. A., Ordway J. I., 1995, AJ, 109,2169
Huenemoerder D. P., Ramsey L. W., 1987, ApJ, 319, 392
Jeffries R. D., 1993, MNRAS, 262, 369
Landman D. A., Mongillo M., 1979, ApJ, 230, 581
Leitzinger M. et al., 2016, MNRAS, 463, 965
López-santiago J., Montes D., Fernández-Figueroa M. J., Ramsey L. W., 2003, A&A, 411, 489
Messina S., 2008, A&AS, 480, 495
Mittag M., Hempelmann A., González-Pérez J. N., Schmitt J. H. M. M., 2010, Adv. Astron., 2010, 6
Montes D., Fernández-Figueroa M. J., Cornide M., de Castro E., 1996, A&A, 312, 221M
Montes D. et al., 2000, A&AS, 146, 103
Montes D., Fernández-Figueroa M. J., De Castro E., Sanz-Forcada J., 1997, A&AS, 125, 263
Montes D., Saar S. H., Collier Cameron A., Unruh Y. C, 1999, MNRAS, 305, 45
Montes D., Sanz-Forcada J., Fernández-Figueroa M. J., Lorente R., 1996, A&A, 310, L29
Popper D. M., 1988, AJ, 95, 1242
Reglero V., Gimenez A., Estela A., 1990, A&A, 231, 375
Rodonò M., Lanza A. F., Becciani U., 2001, A&A, 371, 174
Rodonò M., Lanza A. F., Catalano S., 1995, A&A, 301,75
Strassmeier K. G., Fekel F. C., 1990, A&A, 230, 389
Schmitt J. H. M. M. et al., 2014, Astron. Nachr., 335, 787
Schrijver C. J., Zwaan C., 2000, Solar and stellar magnetic activity. Cambridge Univ. Press, Cambridge
Wolter U., Robrade J., Schmitt J. H. M. M., Ness J. U., 2008, MNRAS, 478, L11
Xiang Y. et al., 2020, MNRAS, 492, 3647
Zhang L.-Y., Gu S.-H., 2008, A&A, 487, 709
Zhang L. Y., Pi Q. F., Han X. M. L., Chang L., Wang D. M., 2016, MNRAS, 459, 854

Zhao G., Li H.-B., 2001, ChJAA, 1, 555

Zirin H., 1988, Astrophysics of the Sun. Cambridge Univ. Press, Cambridge

APPENDIX A: EW MEASUREMENTS FOR THE SUBTRACTION OF CHROMOSPHERIC ACTIVITY INDICATORS

This paper has been typeset from a TEX/LATEX file prepared by the author.

Table A1. EW measurements for the subtraction profiles of the Ca II λ8662, Ca II λ8542, λ8498, H$_\alpha$, and H$_\beta$ lines, and the ratios of EW(λ8542)/EW(λ8498) and E$_{H\alpha}$/E$_{H\beta}$.

Phase	EW(Å)					$\frac{EW(\lambda 8542)}{EW(\lambda 8498)}$	$\frac{E_{H\alpha}}{E_{H\beta}}$
	Ca II λ8662	Ca II λ8542	Ca II λ8498	H$_\alpha$	H$_\beta$		
			1998 Mar, Xinglong 2.16 m				
0.776	0.697±0.045	0.810±0.015	...	0.692±0.019	...	...	...
0.785	0.664±0.017	0.787±0.013	...	0.709±0.011	...	...	...
			2000 Feb, Xinglong 2.16 m				
0.346	0.539±0.015	0.736±0.015	0.476±0.012	0.842±0.015	...	1.55	...
0.350	0.560±0.012	0.788±0.019	0.509±0.005	0.867±0.013	...	1.55	...
			2004 Feb, Xinglong 2.16 m				
0.341	0.567±0.018	0.782±0.016	0.428±0.009	0.648±0.012	...	1.83	...
0.734	0.518±0.006	0.833±0.017	0.559±0.018	0.478±0.015	...	1.49	...
0.752	0.492±0.016	0.758±0.011	0.500±0.009	0.563±0.013	...	1.52	...
0.160	0.516±0.011	0.767±0.021	0.510±0.008	0.932±0.019	...	1.50	...
0.380	0.608±0.012	0.856±0.015	0.483±0.008	0.685±0.011	...	1.77	...
0.576	0.557±0.012	0.689±0.020	0.516±0.011	0.452±0.021	...	1.34	...
			2016 Jan, Xinglong 2.16 m				
0.385	0.597±0.018	0.847±0.014	0.541±0.009	0.710±0.018	...	1.57	...
0.598	0.669±0.013	0.751±0.012	0.475±0.008	0.915±0.010	...	1.58	...
0.608	0.682±0.008	0.739±0.024	0.483±0.013	0.822±0.011	...	1.53	...
0.787	0.631±0.017	0.720±0.017	0.440±0.013	0.810±0.011	...	1.64	...
0.798	0.609±0.013	0.750±0.016	0.455±0.012	0.864±0.014	...	1.65	...
0.816	0.610±0.011	0.794±0.018	0.438±0.011	0.896±0.006	...	1.81	...
0.821	0.644±0.020	0.768±0.013	0.446±0.006	0.896±0.010	...	1.72	...
0.214	0.602±0.014	0.757±0.010	0.449±0.014	0.923±0.014	0.208±0.032	1.69	2.29
0.225	0.610±0.009	0.759±0.014	0.466±0.015	0.983±0.009	0.211±0.033	1.63	2.40
0.236	0.644±0.012	0.849±0.019	0.493±0.009	1.249±0.012	0.313±0.004	1.72	2.06
0.241	0.665±0.010	0.890±0.011	0.517±0.008	1.226±0.010	0.290±0.008	1.72	2.18
0.629	0.564±0.013	0.749±0.021	0.465±0.009	0.726±0.009	0.142±0.010	1.61	2.63
0.634	0.566±0.009	0.744±0.011	0.448±0.010	0.718±0.008	0.169±0.012	1.66	2.19
0.838	0.599±0.019	0.778±0.016	0.502±0.012	0.955±0.009	0.237±0.005	1.55	2.08
0.843	0.618±0.017	0.741±0.015	0.456±0.009	0.897±0.015	0.249±0.015	1.63	1.58
0.056	0.540±0.012	0.661±0.012	0.486±0.014	0.600±0.014	0.162±0.044	1.36	1.91
0.061	0.521±0.006	0.684±0.011	0.509±0.010	0.645±0.006	0.192±0.006	1.34	1.73
0.066	0.574±0.013	0.730±0.013	0.522±0.006	0.743±0.011	0.228±0.012	1.40	1.68
0.071	0.562±0.012	0.715±0.019	0.520±0.014	0.854±0.012	0.200±0.010	1.38	2.20
0.251	0.766±0.012	0.944±0.014	0.628±0.011	1.464±0.013	0.396±0.006	1.50	1.91
0.256	0.761±0.007	0.966±0.013	0.621±0.011	1.452±0.013	0.407±0.012	1.56	1.84
0.271	0.730±0.010	0.914±0.015	0.614±0.010	1.350±0.008	0.405±0.007	1.49	1.72
0.276	0.723±0.012	0.916±0.011	0.590±0.018	1.338±0.009	0.405±0.013	1.55	1.70
			2017 Apr, Weihai 1 m				
0.344	0.670±0.023	0.693±0.021	0.427±0.016	0.819±0.011	...	1.62	...
0.546	0.686±0.026	0.738±0.015	0.504±0.012	0.629±0.015	...	1.46	...
0.555	0.692±0.024	0.740±0.024	0.518±0.014	0.654±0.007	...	1.43	...
0.564	0.720±0.023	0.751±0.025	0.523±0.015	0.697±0.015	...	1.44	...
0.584	0.713±0.025	0.736±0.015	0.525±0.021	0.685±0.015	...	1.40	...
0.593	0.721±0.021	0.747±0.020	0.558±0.019	0.709±0.026	...	1.34	...
0.601	0.658±0.022	0.674±0.021	0.520±0.026	0.692±0.012	...	1.30	...
			2017 Apr, TIGRE 1.2 m				
0.625	0.780±0.021	0.864±0.019	0.575±0.024	0.614±0.024	0.128±0.015	1.50	2.47
0.635	0.766±0.020	0.885±0.020	0.535±0.030	0.620±0.030	0.120±0.017	1.65	2.66
0.644	0.694±0.019	0.791±0.023	0.579±0.029	0.634±0.029	...	1.37	...
0.652	0.699±0.021	0.818±0.021	0.560±0.026	0.651±0.026	0.111±0.013	1.46	3.02
0.661	0.689±0.020	0.879±0.025	0.572±0.036	0.734±0.036	0.130±0.011	1.54	2.91
0.670	0.760±0.016	0.830±0.022	0.529±0.030	0.656±0.030	0.122±0.017	1.57	2.77
0.687	0.749±0.017	0.831±0.023	0.560±0.021	0.681±0.021	...	1.48	...
0.832	0.784±0.021	0.837±0.020	0.587±0.014	0.730±0.014	0.136±0.015	1.43	2.77
0.063	0.784±0.023	0.865±0.018	0.620±0.020	0.600±0.012	0.172±0.013	1.40	1.80
0.072	0.727±0.019	0.840±0.019	0.638±0.020	0.680±0.008	0.172±0.010	1.32	2.04
0.081	0.755±0.023	0.941±0.017	0.663±0.019	0.816±0.020	0.203±0.009	1.42	2.07

Table A1 – *continued*

Phase	EW(Å)					$\frac{EW(\lambda 8542)}{EW(\lambda 8498)}$	$\frac{E_{H\alpha}}{E_{H\beta}}$
	Ca II λ8662	Ca II λ8542	Ca II λ8498	H$_\alpha$	H$_\beta$		
0.091	0.857±0.024	0.960±0.019	0.684±0.018	0.800±0.012	0.194±0.011	1.40	2.13
0.102	0.895±0.019	1.019±0.023	0.704±0.023	0.857±0.013	0.243±0.013	1.45	1.82
0.243	0.868±0.016	0.978±0.018	0.624±0.012	1.042±0.012	0.254±0.012	1.57	2.11
0.256	0.886±0.018	0.962±0.021	0.617±0.017	1.008±0.017	0.235±0.011	1.56	2.21
0.270	0.842±0.021	0.930±0.017	0.674±0.022	0.951±0.022	0.223±0.012	1.38	2.20
0.299	0.819±0.015	0.917±0.023	0.628±0.018	0.818±0.018	0.170±0.015	1.46	2.48
0.452	0.689±0.020	0.840±0.022	0.590±0.020	0.556±0.011	0.122±0.011	1.42	2.35
0.693	0.751±0.018	0.840±0.021	0.569±0.021	0.755±0.021	0.157±0.013	1.48	2.48
0.701	0.775±0.013	0.851±0.016	0.591±0.021	0.766±0.041	...	1.44	...
0.714	0.732±0.022	0.860±0.019	0.582±0.025	0.751±0.035	0.142±0.012	1.48	2.73
0.722	0.763±0.019	0.858±0.014	0.581±0.016	0.765±0.036	0.138±0.017	1.48	2.86
0.863	0.726±0.017	0.891±0.015	0.552±0.013	0.645±0.013	0.131±0.013	1.61	2.54
0.872	0.747±0.021	0.920±0.017	0.574±0.027	0.616±0.027	0.114±0.015	1.60	2.78
0.880	0.694±0.018	0.834±0.023	0.578±0.016	0.591±0.016	0.112±0.011	1.44	2.72
0.888	0.695±0.013	0.866±0.021	0.577±0.021	0.589±0.021	0.123±0.013	1.50	2.47
0.896	0.685±0.019	0.858±0.025	0.548±0.013	0.596±0.013	0.105±0.010	1.57	2.93
0.904	0.680±0.020	0.849±0.016	0.563±0.015	0.565±0.015	0.128±0.011	1.51	2.27
0.913	0.704±0.024	0.839±0.021	0.564±0.021	0.570±0.021	0.114±0.013	1.49	2.58
0.924	0.711±0.021	0.854±0.022	0.586±0.011	0.518±0.011	0.115±0.017	1.46	2.32
0.932	0.693±0.021	0.800±0.019	0.584±0.020	0.515±0.013	0.117±0.013	1.37	2.27
0.076	0.710±0.019	0.805±0.018	0.580±0.021	0.512±0.010	0.152±0.012	1.39	1.74
0.084	0.677±0.018	0.819±0.021	0.591±0.018	0.529±0.011	0.148±0.011	1.39	1.84
0.092	0.708±0.017	0.839±0.020	0.578±0.020	0.552±0.009	0.162±0.015	1.45	1.76
0.100	0.717±0.022	0.847±0.019	0.580±0.019	0.570±0.010	0.140±0.010	1.46	2.10
0.108	0.668±0.018	0.852±0.017	0.579±0.022	0.551±0.021	0.172±0.012	1.47	1.65
0.116	0.663±0.020	0.873±0.021	0.600±0.021	0.542±0.016	0.169±0.011	1.46	1.65
0.126	0.697±0.021	0.866±0.020	0.613±0.020	0.549±0.016	0.168±0.013	1.41	1.68
0.134	0.669±0.019	0.949±0.018	0.670±0.019	0.549±0.011	0.187±0.016	1.42	1.51
0.142	0.745±0.020	0.890±0.019	0.581±0.022	0.537±0.010	0.159±0.012	1.53	1.74
	2017 Nov–Dec, Xinglong 2.16 m						
0.298	0.659±0.032	0.810±0.032	0.422±0.014	0.866±0.007	0.168±0.012	1.92	2.65
0.302	0.617±0.016	0.845±0.016	0.414±0.018	0.888±0.019	0.156±0.015	2.04	2.93
0.307	0.678±0.014	0.855±0.014	0.429±0.016	0.860±0.017	0.156±0.015	1.99	2.84
0.719	0.754±0.061	0.931±0.061	0.440±0.015	1.299±0.012	0.208±0.011	2.12	3.22
0.724	0.712±0.044	0.915±0.044	0.456±0.014	1.295±0.012	0.261±0.032	2.01	2.56
0.927	0.728±0.020	1.040±0.020	0.528±0.015	0.434±0.015	0.024±0.008	1.97	9.32
0.932	0.708±0.008	1.010±0.008	0.498±0.016	0.404±0.010	0.015±0.004	2.03	13.88
0.172	0.647±0.021	0.864±0.021	0.424±0.013	0.937±0.009	0.204±0.011	2.04	2.37
0.177	0.625±0.006	0.873±0.006	0.423±0.014	0.927±0.012	0.156±0.022	2.06	3.06
0.182	0.660±0.012	0.869±0.012	0.433±0.014	0.873±0.008	0.153±0.018	2.01	2.94
0.378	0.683±0.013	0.823±0.013	0.428±0.014	0.740±0.020	0.124±0.011	1.92	3.08
0.383	0.640±0.002	0.829±0.002	0.432±0.012	0.777±0.012	0.188±0.010	1.92	2.13
0.388	0.640±0.024	0.838±0.024	0.445±0.018	0.783±0.013	0.190±0.013	1.88	2.12
0.393	0.649±0.007	0.873±0.007	0.446±0.013	0.836±0.005	0.200±0.025	1.96	2.15
0.590	0.704±0.008	1.048±0.008	0.490±0.018	0.956±0.008	0.211±0.010	2.14	2.33
0.595	0.721±0.008	1.073±0.008	0.473±0.014	0.970±0.012	0.193±0.008	2.27	2.59
0.600	0.732±0.008	1.071±0.008	0.505±0.016	0.991±0.009	0.196±0.007	2.12	2.61
0.791	0.716±0.030	0.896±0.030	0.437±0.012	1.073±0.009	0.250±0.023	2.05	2.21
0.796	0.806±0.056	0.945±0.056	0.459±0.014	1.062±0.011	0.261±0.020	2.06	2.10
0.801	0.712±0.021	0.915±0.021	0.478±0.013	1.107±0.016	0.271±0.047	1.91	2.10
0.806	0.754±0.041	0.891±0.041	0.430±0.015	1.173±0.012	0.260±0.011	2.07	2.32
0.81	0.781±0.048	0.899±0.048	0.391±0.017	1.231±0.007	0.280±0.013	2.30	2.27
0.007	1.085±0.017	0.950±0.008	0.482±0.013	0.956±0.018	0.287±0.021	1.97	1.72
0.012	1.045±0.011	0.908±0.009	0.496±0.012	0.940±0.008	0.274±0.013	1.83	1.77
0.017	1.003±0.023	0.884±0.011	0.498±0.012	0.956±0.021	0.302±0.017	1.78	1.63